4D MAP Image Reconstruction Incorporating Organ Motion

Jacob Hinkle[1], P. Thomas Fletcher[1], Brian Wang[2], Bill Salter[2], and Sarang Joshi[1]

[1] Scientific Computing and Imaging Institute, University of Utah
Salt Lake City, Utah
[2] Huntsman Cancer Institute, University of Utah, Salt Lake City, Utah

Abstract. Four-dimensional respiratory correlated computed tomography (4D RCCT) has been widely used for studying organ motion. Most current algorithms use binning techniques which introduce artifacts that can seriously hamper quantitative motion analysis. In this paper, we develop an algorithm for tracking organ motion which uses raw time-stamped data and simultaneously reconstructs images and estimates deformations in anatomy. This results in a reduction of artifacts and an increase in signal-to-noise ratio (SNR). In the case of CT, the increased SNR enables a reduction in dose to the patient during scanning. This framework also facilitates the incorporation of fundamental physical properties of organ motion, such as the conservation of local tissue volume. We show in this paper that this approach is accurate and robust against noise and irregular breathing for tracking organ motion. A detailed phantom study is presented, demonstrating accuracy and robustness of the algorithm. An example of applying this algorithm to real patient image data is also presented, demonstrating the utility of the algorithm in reducing artifacts.

1 Introduction

Four-dimensional respiratory-correlated computed tomography (4D RCCT) has been widely used for studying organ motion. The current standard practice is to use phase binned images [1]. However, the phase binning algorithm assumes that the patient has a periodic breathing pattern. When the patient's breathing is irregular, this assumption breaks down and significant image artifacts like those shown in Fig. 1 are introduced. In a recent extensive study, Yamamoto et al. [2] found that 90% of 4D RCCT patients had at least one artifact. Amplitude binning algorithms have been developed as a way to alleviate these artifacts by assuming that the underlying anatomical configuration is correlated to the amplitude of the breathing signal. This method reduces binning artifacts but since data is not acquired at all breathing amplitudes the images often have some missing slices [1]. Deformable image registration has been shown to be useful in tracking organ motion in artifact-free 4D RCCT images [3]. Such methods may be used with either phase or amplitude binned images, but are challenged in the presence of binning artifacts.
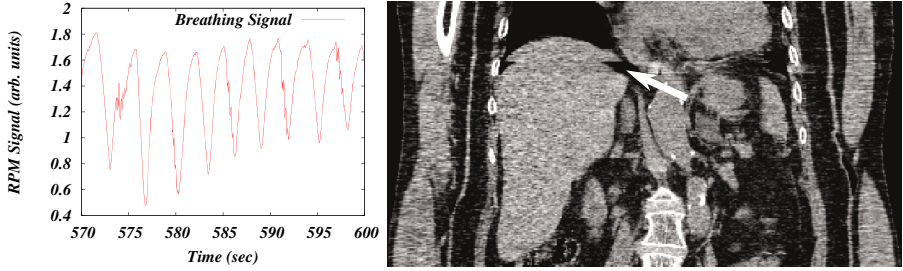
Fig. 1. Non-periodic patient breathing pattern (left) and image artifacts introduced by phase binning (right)

In this paper, we develop a maximum a posteriori (MAP) algorithm for tracking organ motion that uses raw time-stamped data to reconstruct the images and estimate deformations in anatomy simultaneously. The algorithm eliminates artifacts as it does not rely on a binning process and increases signal-to-noise ratio (SNR) by using all of the collected data. In the case of CT, the increased SNR provides the opportunity to reduce dose to the patient during scanning. This framework also facilitates the incorporation of fundamental physical properties such as the conservation of local tissue volume during the estimation of the organ motion. We show that this formulation is accurate and robust against noise and irregular breathing for tracking organ motion and reducing artifacts in a detailed phantom study. An improvement in image quality is also demonstrated by application of the algorithm to data from a real liver stereotactic body radiation therapy patient.

1.1   Previous Work in Motion Artifact Elimination

Previous attempts at reducing 4D RCCT motion artifacts do not offer all the advantages of our proposed method, which incorporates a fully diffeomorphic motion model into the reconstruction process. For instance, Yu and Wang [4] model rigid 2D motion during acquisition to alleviate in-plane artifacts in fan-beam CT. Their motion model is not valid for imaging of the torso, where respiratory-induced motion causes highly non-linear deformation with a significant component in the superior-inferior direction. Another method, presented by Li et al. [5], reconstructs a full 4D time-indexed image using a B-spline motion model and a temporal smoothing condition. Zeng et al. [6] and Li et al. [7] present other B-spline-based methods that require an artifact-free reference image (such as a breath-hold image) in addition to a 4D fan-beam or cone-beam scan. These approaches address difficulties caused by slowly-rotating cone-beam scanners. However the acquisition of an artifact-free reference image is impractical for many radiotherapy patients. While the B-spline model guarantees smooth deformations, it cannot guarantee the diffeomorphic properties for large deformations ensured by our method and it does not directly enforce local conservation of tissue volume. Erhardt et al. [8] reconstruct 3D images at arbitrary amplitudes

by interpolating each slice from those collected at nearby amplitudes and then stacking them. Two slices are used to interpolate a slice at the desired amplitude using an optical flow algorithm, so only 2D motion can be estimated. Recently, Rit et al. [9] have used a 4D cone-beam scan to estimate organ motion using an optical flow approach. The motion estimate is then used to correct for organ motion during subsequent 3D scans on the fly. This method may be useful in reducing artifacts in a 3D image, but the optical flow model, like the B-Spline model, does not ensure diffeomorphic incompressible motion estimates.

As early as 1991, Song and Leahy [10] used an incompressible optical flow method for image registration. Rohlfing et al. [11] use a spline-based model which penalizes tissue compression to perform incompressible image registration. Saddi et al. [12] study incompressible fluid-based registration of liver CT. Their approach requires solution of Poisson's equation via a multigrid method at each iteration. An efficient Fourier method of incompressible projection similar to the one presented in this paper is presented by Stam [13]. His approach applies a result from the continuous domain to discrete data without alteration, while our method directly accommodates the discrete nature of our image data. Despite these efforts in image registration, the incompressible nature of internal organs has not previously been incorporated into the image reconstruction process.

2   RCCT Data Acquisition

During a typical 4D RCCT fan-beam scan, the patient passes through the scanner on an automated couch that pauses at regular intervals to collect data. At each couch position slices are acquired repeatedly 15–20 times. Each slice is acquired by collecting a series of projections at different angles. The slices are then reconstructed individually using filtered back-projection [14]. The speed of acquisition of each slice is dependent on the scanner and for current generation multi-slice scanners is generally on the order of 0.5 s. The X-ray detection process used to acquire slices is subject to Poisson noise [15]. However, at the x-ray tube currents typically used in clinical practice the signal is strong enough that the noise is approximately Gaussian. The patient's breathing is monitored during acquisition using an external surrogate for internal organ motion. The resulting breathing trace, $a(t)$, is used to tag the acquired projection retrospectively with a breathing amplitude. For the studies presented in this paper breathing is monitored via the Real-time Position Management (RPM) system (Varian Oncology Systems, Palo Alto, CA), which uses a camera to track infrared-reflective markers attached to the patient's torso. The methods presented herein are general and can be applied to signals recorded by breathing monitoring systems such as spirometry [16] or chest circumference tracking [17]. Although developed with 4D RCCT of liver as the main application, the methods may be applied to other motion such as cardiac using the ECG signal in place of a breathing monitor.

3   4D Imaging Model

The 4D image reconstruction problem is to estimate the time-indexed image $I(t, x)$ that best represents the patient's anatomy during image acquisition. In order to obtain a maximum a posteriori estimate of organ motion we derive the data likelihood and define a prior model incorporating the physical constraints. We estimate the 4D image that maximizes the posterior probability combining the data likelihood and the prior.

CT image acquisition is described by a projection operator, P_θ, which can represent fan-beam or cone-beam projections at angle θ. At sufficiently high signal-to-noise ratio, the acquisition of a single projection p_i is subject to Gaussian noise of variance σ^2. The data log-likelihood then becomes

$$\mathcal{L}(\{p_i\}|I(t,\boldsymbol{x})) = -\frac{1}{2\sigma^2} \sum_i \int_s |P_{\theta_i}\{I(t_i,\boldsymbol{x})\}(s) - p_i(s)|^2 \, ds, \tag{1}$$

where the integration with respect to s is over a one or two-dimensional domain depending on the projection operator used.

Due to the sparsity of the imaging data, the full 4D image reconstruction problem is ill-posed, so it is necessary to constrain the estimation. We assume that no metabolic changes or local tissue density variations occur during acquisition and that the only dynamic process is the motion of the anatomy due to breathing. Under this assumption, the 4D image is described by a time-indexed deformation field and a single representative static 3D image, $I_0(x)$, as

$$I(t, \boldsymbol{x}) = I_0(h(t, \boldsymbol{x})), \tag{2}$$

where for each time t, $h(t, \cdot)$ is a volume-preserving diffeomorphic deformation capturing the respiratory-induced motion of the underlying anatomy.

We assume that organ motion is correlated with breathing amplitude, so the deformation may be indexed by amplitude only. Under this assumption the deformations take the form $h(a(t), \boldsymbol{x})$. The velocity of a point in the patient's anatomy is then described by the ordinary differential equation

$$\frac{d}{dt}h(a(t), \boldsymbol{x}) = v(a(t), h(a(t), \boldsymbol{x}))\frac{da}{dt}, \tag{3}$$

where v is indexed by amplitude and may be thought of as a velocity with respect to changes in amplitude rather than time. The deformation from zero amplitude to any other amplitude is given by the associated integral equation

$$h(a, \boldsymbol{x}) = \boldsymbol{x} + \int_0^a v(a', h(a', \boldsymbol{x}))da'. \tag{4}$$

If the velocities are constrained to be smooth, this formulation guarantees that the resulting estimates of patient anatomy are at all times diffeomorphic to one another. This is important as it ensures that organs do not tear or disappear during breathing [18]. The diffeomorphic deformations provide a one-to-one

correspondence between points in images from different breathing amplitudes, enabling tracking of tissue trajectories. We enforce smoothness by introducing a prior on the velocities via a Sobolev norm $\|v\|_V^2$, defined by

$$\|v\|_V^2 = \langle v, v \rangle_V = \int_0^1 \int_{\boldsymbol{x} \in \Omega} \|Lv(a, \boldsymbol{x})\|_{\mathbb{R}^3}^2 d\boldsymbol{x} da, \tag{5}$$

where L is a differential operator chosen to reflect physical tissue properties. Although in this paper we use a homogeneous operator, L can be spatially-varying reflecting the different material properties of the underlying anatomy.

Deformations defined by the flow along smoothly-varying vector fields as described in Eq. 3 have been well studied [19]. In particular, if the divergence of the velocity field is zero the resulting deformation is guaranteed to preserve volume locally and have unit Jacobian determinant. This is a necessary constraint when modeling the breathing induced motion of incompressible fluid-filled organs such as liver. In fact, if L is the Laplacian operator and the velocities are constrained to be divergence-free, the velocities simulate Stokes flow of an incompressible viscous fluid [20].

With the data log-likelihood and the prior model described above, the log-posterior probability of observing our data becomes

$$\mathcal{L}(I_0, v | p_i) = -\|v(a)\|_V^2 - \frac{1}{2\sigma^2} \sum_i \int_s |P_{\theta_i}\{I_0 \circ h(a_i, x, y, z_i)\}(s) - p_i(s)|^2 ds,$$

$$\text{subject to div } v = 0. \quad (6)$$

4   Model Estimation

Having defined the posterior, the 4D image reconstruction problem is to estimate the image and deformations parameterized by the velocity field that maximize Eq. 6,

$$(\hat{I}_0, \hat{v}) = \underset{I_0, v}{\operatorname{argmax}} \mathcal{L}(I_0, v | p_i) \qquad \text{subject to div } v = 0. \tag{7}$$

A MAP estimate that maximizes Eq. 6 is obtained via an alternating iterative algorithm which at each iteration updates the estimate of the deformation in a gradient ascent step then updates the image using the associated Euler-Lagrange equation. The continuous amplitude-indexed velocity field is discretized by a set of equally-spaced amplitudes a_k with the associated velocities v_k, with spacing Δa. Note that this amplitude discretization is independent of the amplitudes at which data is acquired. The deformation from amplitude a_k to a_{k+1} is approximated by the Euler integration of Eq. 4,

$$h(a_{k+1}, \boldsymbol{x}) = h(a_k, \boldsymbol{x}) + v_k(h(a_k, \boldsymbol{x})) \tag{8}$$

and the deformation for an amplitude a_i between a_k and a_{k+1} is linearly interpolated as

$$h(a_i, \boldsymbol{x}) = h(a_k, \boldsymbol{x}) + \frac{a_i - a_k}{\Delta a} v_k(h(a_k, \boldsymbol{x})). \tag{9}$$

Note that higher order integration schemes such as Runge-Kutta may also be used in place of the simpler Euler method.

The first variation of Eq. 6 with respect to v_k under the inner product in Eq. 5 is given by

$$\delta_{v_k}\mathcal{L}(I_0, v_k|p_i) = -2v_k - \frac{1}{\sigma^2}(L^\dagger L)^{-1}\sum_i P_{\theta_i}^\dagger\left(P_{\theta_i}\{I_0 \circ h(a_i, \cdot)\} - p_i\right)b_i(k, \cdot),$$
(10)

where b_i is the contribution to the variation due to a single projection and $P_{\theta_i}^\dagger$ is the adjoint of the projection operator, which acts by backprojecting the data discrepancy back into the 3D volume. The adjoint operators for various imaging geometries have been well studied. For parallel-beam CT geometry, the adjoint projection operator is the familiar backprojection operator. Conventional filtered backprojection CT slice reconstruction involves applying the adjoint operator, after filtering the 1D data [14]. Let $I_k(\boldsymbol{x}) = I_0 \circ h(a_k, \boldsymbol{x})$ be the 3D reference image pushed forward to amplitude a_k, the factors b_i are given by

$$b_i(k, \boldsymbol{x}) = \begin{cases} 0 & a_i \leq a_k \\ \frac{a_i - a_k}{\Delta a}\nabla I_k(\boldsymbol{x} + \frac{a_i - a_k}{\Delta a}v_k(\boldsymbol{x})) & a_k < a_i \leq a_{k+1} \\ \left|D(h_{a_{k+1}} \circ h_{a_i}^{-1})(\boldsymbol{x})\right|\nabla I_k(\boldsymbol{x} + v_k(\boldsymbol{x})) & a_i > a_{k+1}. \end{cases}$$
(11)

If the deformations are constrained to be incompressible, implying that the Jacobian determinant is unity, this simplifies to

$$b_i(k, \boldsymbol{x}) = \begin{cases} 0 & a_i \leq a_k \\ \frac{a_i - a_k}{\Delta a}\nabla I_k(\boldsymbol{x} + \frac{a_i - a_k}{\Delta a}v_k(\boldsymbol{x})) & a_k < a_i \leq a_{k+1} \\ \nabla I_k(\boldsymbol{x} + v_k(\boldsymbol{x})) & a_i > a_{k+1}. \end{cases}$$
(12)

Following the approach of Beg et al. [21], efficient computation of $(L^\dagger L)^{-1}$ is implemented in the Fourier domain, requiring only a matrix multiplication and Fourier transforms of v_k at each iteration of the algorithm.

The Helmholtz-Hodge decomposition allows us to implement the incompressibility constraint by simply projecting the unconstrained velocity fields onto the space of divergence-free vector fields at each iteration of the algorithm [22]. In order to efficiently implement the Helmholtz-Hodge decomposition of a time-varying velocity field, we use the discrete divergence operator as it operates in Fourier domain. We write the discrete Fourier transform of a central difference approximation to the derivative of a function f as

$$\text{DFT}\{\Delta_x f\}(\omega) = \text{DFT}\left\{\frac{f(x + k_x) - f(x - k_x)}{2k_x}\right\}(\omega) = \frac{i}{2k_x}\sin\omega\,\text{DFT}\{f\}(\omega).$$
(13)

In the Fourier domain the divergence of a vector field takes the following form:

$$\text{DFT}\{\text{div}\,v\}(\boldsymbol{\omega}) = W(\boldsymbol{\omega}) \cdot \text{DFT}\{v\}(\boldsymbol{\omega}),$$
(14)

where

$$W(\boldsymbol{\omega}) = \frac{i}{2} \begin{pmatrix} \frac{1}{k_x}\sin\frac{\omega_x}{N_x} \\ \frac{1}{k_y}\sin\frac{\omega_y}{N_y} \\ \frac{1}{k_z}\sin\frac{\omega_z}{N_z} \end{pmatrix}. \tag{15}$$

This allows us to remove the divergent component easily in Fourier space via the projection

$$\mathrm{DFT}\{v\}(\boldsymbol{\omega}) \mapsto \mathrm{DFT}\{v\}(\boldsymbol{\omega}) - \frac{W(\boldsymbol{\omega}) \cdot \mathrm{DFT}\{v\}(\boldsymbol{\omega})}{\|W(\boldsymbol{\omega})\|^2_{\mathbb{C}^3}} W(\boldsymbol{\omega}). \tag{16}$$

Since the operator $(L^\dagger L)^{-1}$ is implemented in the Fourier domain there is little computational overhead in performing this projection at each iteration of the algorithm described in Sec. 4.

The first variation of Eq. 6 with respect to I_0 is

$$\delta_{I_0}\mathcal{L}(I_0, v|p_i) = \frac{1}{\sigma^2}\sum_i |Dh^{-1}(a_i, \cdot)| \left(P^\dagger_{\theta_i} P_{\theta_i}\{I_0 \circ h(a_i, \cdot)\} - P^\dagger_{\theta_i} p_i \right) \circ h^{-1}(a_i, \cdot). \tag{17}$$

If organ motion is slow compared to single slice acquisition time, individual slices can be reconstructed with minimal motion artifacts using filtered back projection. In this case the 4D image is estimated from the reconstructed 2D slices $S_i(x, y)$. Note that this assumption holds reasonably well in the case of 4D RCCT. Under the slow motion assumption, the velocity field variation becomes

$$\delta_{v_k}\mathcal{L}(I_0, v_k|p_i) = -2v_k - \frac{1}{\sigma^2}(L^\dagger L)^{-1}\sum_i (I_0 \circ h(a_i, \cdot) - S_i)\, b_i(k, \cdot). \tag{18}$$

For slice data, S_i, and an incompressible deformation estimate Eq. 17 is solved by the mean of the deformed data,

$$\hat{I}_0(\boldsymbol{x}) = \frac{1}{N}\sum_{i, h^{-1}(a_i, \boldsymbol{x})_z = z_i} S_i \circ h^{-1}(a_i, \boldsymbol{x}), \tag{19}$$

which is equivalent to solving the Euler-Lagrange equation for Eq. 6.

Algorithm 1. Pseudocode for 4D reconstruction of slice data

$I_0 \leftarrow 0$
for each k **do**
    $v_k \leftarrow 0$
end for
repeat
    $I_0 \leftarrow \frac{1}{N}\sum S_i \circ h^{-1}(a_i, \boldsymbol{x})$
    for each k **do**
        $v_k \leftarrow v_k + \epsilon\delta_{v_k}\mathcal{L}(I_0, v_k)$
    end for
    Perform divergence-free projection on each v_k
until algorithm converges or maximum number iterations reached

---

Note that as soon as the velocity field is updated, the image estimate must also be updated. The change of image estimate in turn alters the velocity gradients leading to a joint estimation algorithm in which, at each iteration, the velocity fields are updated and then the image recalculated.

Algorithm 1 summarizes the 4D reconstruction procedure for slice data. The velocity fields are initialized to zero, so that the initial estimate of the base image is simply the result of averaging all of the data. This yields a quite blurry image that sharpens upon further iterations as the motion estimate improves.

5   Results

5.1   Phantom Study

In order to validate the accuracy of the 4D reconstruction algorithm, a phantom study was performed using the CIRS anthropomorphic thorax phantom (CIRS Inc., Norfolk, VA) and a GE Lightspeed RT scanner (GE Health Care, Waukesha, WI). The phantom includes a simulated chest cavity with a 2 cm spherical object representing a tumor that is capable of moving in three dimensions. A chest marker is also included in the phantom which moves in a pattern synchronized to the tumor and allows simulation of a real patient 4D RCCT scan. The scans used in this study were driven to simulate a breathing trace collected from a real patient.

Figure 2 shows the experimental setup, with the recorded RPM trace and the stationary spherical CIRS lung tumor phantom imaged with helical CT. The 4D phase binned dataset generated by the GE Advance Workstation is shown in the top row of Fig. 3. Notice the binning artifacts including mismatched slices in the phase binned data when compared with the image of the stationary phantom. Also shown in Fig. 3 bottom row are images from an amplitude binned dataset at peak-inhale, mid-range amplitude, and peak-exhale. The images do not show signs of mismatched slices and more closely resemble the static phantom image but suffer from missing data artifacts.

Because we did not have access to the raw projection data, we applied the slow motion assumption described in the previous section when using the CINE
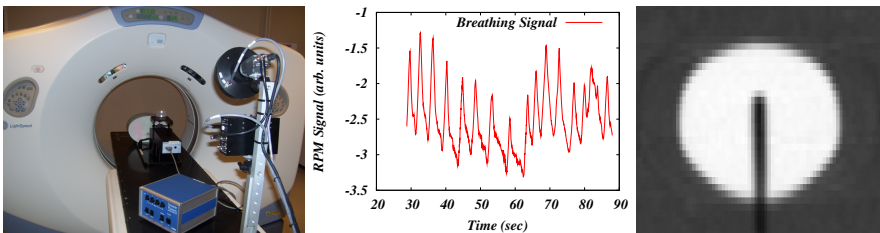

Fig. 2. (left) CIRS phantom during scan setup with Varian RPM camera and GE Lightspeed RT scanner, (center) breathing trace recorded during phantom acquisition and (right) a helical CT scan of the stationary phantom
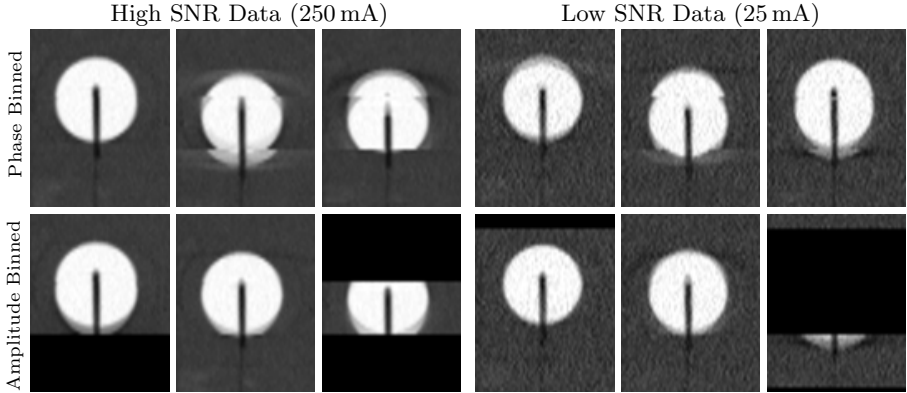
Fig. 3. Binned images of the moving CIRS phantom. The top row shows phase binned images at three different phases for the high SNR data (left) and the low SNR (10% tube current) data (right). The bottom row shows amplitude binned images at end-inhale, mid-range, and end-exhale amplitudes for both the high and low SNR data.

slice data along with the recorded RPM trace in the 4D reconstruction algorithm. In order to demonstrate robustness against noise, an initial scan was taken with an X-ray tube current of 250 mA then repeated with a tube current of 25 mA. Shown in Fig. 4 are the 4D reconstructed images generated using the same raw data as the phase and amplitude binned images in Fig. 3. Notice that the reconstructed image does not have any artifacts associated with either the
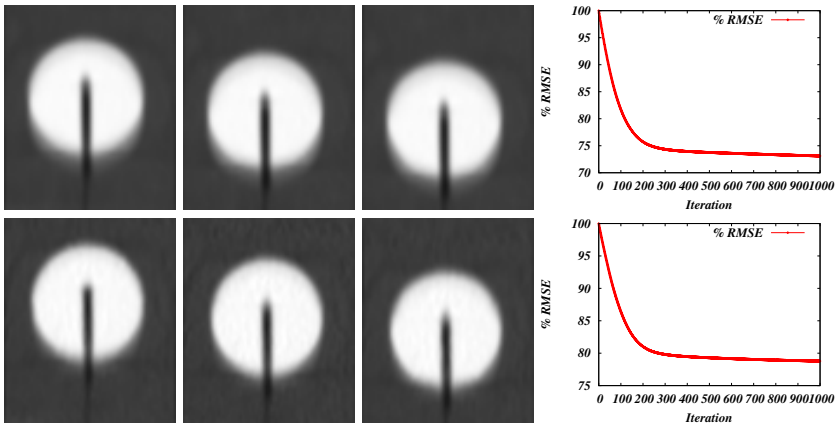
Fig. 4. 4D reconstructed images of the phantom at end-inhale, mid-range, and end-exhale amplitudes. The top row shows the 4D reconstruction of the high SNR data, while the bottom row shows that of the low SNR data. Also shown are plots of the posterior indicating the convergence of the algorithm.
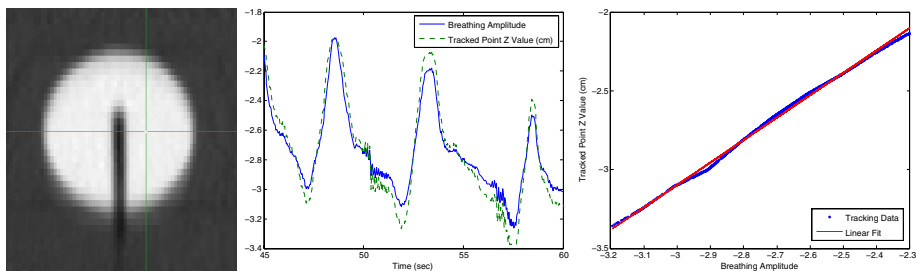
Fig. 5. Tracked point (left) with RPM signal and superior-inferior (z) coordinate (center) and plot of tracked point z coordinate versus RPM signal (right) showing strong linear correlation

phase binning or amplitude binning. Notice also the increase in SNR in the 4D reconstructed images. Reconstructed 4D images from 25 mA data have higher signal-to-noise ratio (SNR=76.5) than binned images reconstructed using 250 mA data (SNR=53.9). The similarity in images between the two 4D reconstructions shows the robustness of the image estimation to increasing noise.

To validate the estimated deformation model, a single point at the center of the phantom indicated by the cross hair in Fig. 5 was tracked by integrating the estimated velocity fields according to Eq. 4. The physical construction of the phantom dictates that the superior-inferior displacement is linearly correlated to the RPM signal. Shown in Fig. 5 is a plot of the estimated displacements versus the RPM signal. Notice the excellent linear correlation ($r = 0.9988$) between them, validating the deformation estimation process.

5.2   Real Patient Study

The 4D reconstruction algorithm was also applied to data collected from a real patient undergoing hypo-fractionated radiation therapy treatment of the liver at the Huntsman Cancer Institute at the University of Utah. A comparison between phase
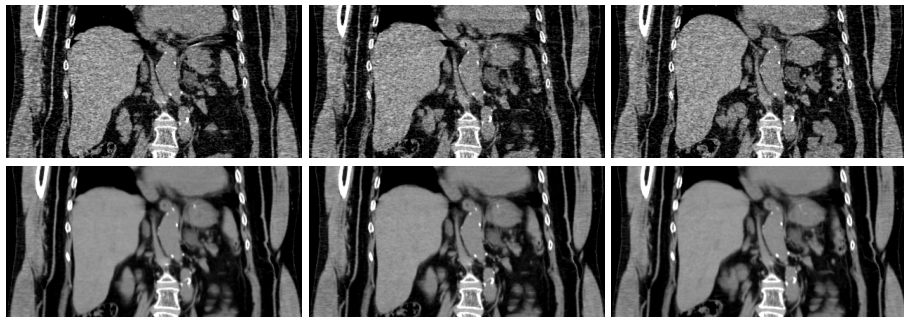
Fig. 6. Phase binned images (top) along with 4D reconstructed images (bottom) at peak-exhale, mid-range, and peak-inhale
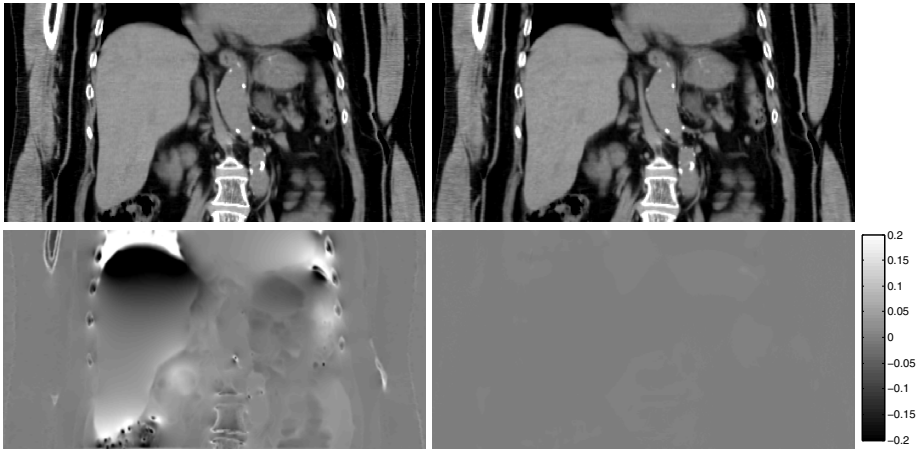
Fig. 7. 4D reconstructed images and log Jacobian determinant images (bottom) for compressible flow reconstruction (left) and with incompressibility constraint (right). Negative log Jacobian values indicate local compression, while positive values indicate expansion.

binning and the 4D reconstruction is shown in Fig. 6. In addition to improving SNR, slice mismatch artifacts are absent in the 4D reconstructed image.

The 4D reconstruction algorithm was run with and without the incompressibility constraint. Analysis of the incompressibility projection is shown in Fig. 7. The reconstructed images are extremely similar, while the Jacobian maps are quite different. In particular, it is seen that without the incompressibility constraint, the estimated motion indicates compression and expansion of the top and bottom of the liver, while the incompressible reconstruction shows no local expansion or contraction. This illustrates the fact that although the two methods produce very similar images, the motion estimates are quite different. Given that liver is a blood-filled organ, physiologically it does not undergo any appreciable local changes in volume due to breathing. This exemplifies the necessity of incorporating incompressibility into the reconstruction process.

References

1. Abdelnour, A.F., Nehmeh, S.A., Pan, T., Humm, J.L., Vernon, P., Schöder, H., Rosenzweig, K.E., Mageras, G.S., Yorke, E., Larson, S.M., Erdi, Y.E.: Phase and amplitude binning for 4D-CT imaging. Phys. Med. Biol. 52(12), 3515–3529 (2007)
2. Yamamoto, T., Langner, U., Billy, W., Loo, J., Shen, J., Keall, P.J.: Retrospective analysis of artifacts in four-dimensional CT images of 50 abdominal and thoracic radiotherapy patients. Int. J. Radiat. Oncol. Biol. Phys. 72(4), 1250–1258 (2008)
3. Pevsner, A., Davis, B., Joshi, S., Hertanto, A., Mechalakos, J., Yorke, E., Rosenzweig, K., Nehmeh, S., Erdi, Y.E., Humm, J.L., Larson, S., Ling, C.C., Mageras, G.S.: Evaluation of an automated deformable image matching method for quantifying lung motion in respiration-correlated CT images. Med. Phys. 33(2), 369–376 (2006)

4. Yu, H., Wang, G.: Data consistency based rigid motion artifact reduction in fanbeam CT. IEEE Trans. Med. Imag. 26(2), 249–260 (2007)
5. Li, T., Schreibmann, E., Thorndyke, B., Tillman, G., Boyer, A., Koong, A., Goodman, K., Xing, L.: Radiation dose reduction in four-dimensional computed tomography. Med. Phys. 32(12), 3650–3660 (2005)
6. Zeng, R., Fessler, J.A., Balter, J.M.: Respiratory motion estimation from slowly rotating X-ray projections: Theory and simulation. Med. Phys. 32(4), 984–991 (2005)
7. Li, T., Koong, A., Xing, L.: Enhanced 4D cone-beam CT with inter-phase motion model. Med. Phys. 34(9), 3688–3695 (2007)
8. Ehrhardt, J., Werner, R., Säring, D., Frenzel, T., Lu, W., Low, D., Handels, H.: An optical flow based method for improved reconstruction of 4D CT data sets acquired during free breathing. Med. Phys. 34(2), 711–721 (2007)
9. Rit, S., Wolthaus, J., van Herk, M., Sonke, J.J.: On-the-fly motion-compensated cone-beam CT using an a priori motion model. In: Metaxas, D., Axel, L., Fichtinger, G., Székely, G. (eds.) MICCAI 2008, Part I. LNCS, vol. 5241, pp. 729–736. Springer, Heidelberg (2008)
10. Song, S.M., Leahy, R.M.: Computation of 3-D velocity fields from 3-D cine CT images of a human heart. IEEE Trans. Med. Imag. 10(3), 295–306 (1991)
11. Rohlfing, T., Calvin, R., Maurer, J., Bluemke, D.A., Jacobs, M.A.: Volume-preserving nonrigid registration of MR breast images using free-form deformation with an incompressibility constraint. IEEE Trans. Med. Imag. 22(6), 730–741 (2003)
12. Saddi, K.A., Chefd'hotel, C., Cheriet, F.: Large deformation registration of contrast-enhanced images with volume-preserving constraint. In: Proceedings of International Society for Optical Engineering (SPIE) Conference on Medical Imaging 2007, vol. 6512 (2007)
13. Stam, J.: A simple fluid solver based on the FFT. Journal of Graphics Tools 6(2), 383–396 (2001)
14. Prince, J.L., Links, J.M.: Medical imaging signals and systems. Prentice-Hall, Englewood Cliffs (2006)
15. Guan, H., Gordon, R.: Computed tomography using algebraic reconstruction techniques (ARTS) with different projection access schemes: a comparison study under practical situations. Phys. Med. Biol. 41(9), 1727–1743 (1996)
16. Hoisak, J.D.P., Sixel, K.E., Tirona, R., Cheung, P.C.F., Pignol, J.P.: Correlation of lung tumor motion with external surrogate indicators of respiration. Int. J. Radiat. Oncol. Biol. Phys. 60(4), 1298–1306 (2004)
17. Bosmans, G., van Baardwijk, A., Dekker, A., Öllers, M., Boersma, L., Minken, A., Lambin, P., Ruysscher, D.D.: Intra-patient variability of tumor volume and tumor motion during conventionally fractionated radiotherapy for locally advanced non-small-cell lung cancer: A prospective clinical study. Int. J. Radiat. Oncol. Biol. Phys. 66(3), 748–753 (2006)
18. Joshi, S.C., Miller, M.I.: Landmark matching via large deformation diffeomorphisms. IEEE Trans. Imag. Proc. 9(8), 1357–1370 (2000)
19. Arnold, V.I.: Mathematical Methods of Classical Mechanics, 2nd edn. Springer, Heidelberg (1997)
20. Panton, R.L.: Incompressible Flow, 2nd edn. Wiley-Interscience, Hoboken (1996)
21. Beg, M.F., Miller, M.I., Trouvé, A., Younes, L.: Computing large deformation metric mappings via geodesic flows of diffeomorphisms. Int. J. Comp. Vis. 61(2), 139–157 (2005)
22. Cantarella, J., DeTurck, D., Gluck, H.: Vector calculus and the topology of domains in 3-space. Amer. Math. Monthly 109(5), 409–442 (2002)